



Low-volume magmatism linked to flank deformation on Isla Santa Cruz, Galápagos Archipelago, using cosmogenic ${}^3\text{He}$ exposure and ${}^{40}\text{Ar}/{}^{39}\text{Ar}$ dating of fault scarps and lavas

D. M. Schwartz¹ · K. Harpp² · M. D. Kurz³ · E. Wilson⁴ · R. Van Kirk²

Received: 2 February 2022 / Accepted: 30 May 2022 / Published online: 4 August 2022
© The Author(s) 2022

Abstract

Isla Santa Cruz is a volcanic island located in the central Galápagos Archipelago. The island's northern and southern flanks are deformed by E–W-trending normal faults not observed on the younger Galápagos shields, and Santa Cruz lacks the large summit calderas that characterize those structures. To construct a chronology of volcanism and deformation on Santa Cruz, we employ ${}^{40}\text{Ar}/{}^{39}\text{Ar}$ geochronology of lavas and ${}^3\text{He}$ exposure dating of fault scarps from across the island. The combination of Ar–Ar dating with in situ-produced cosmogenic exposure age data provides a powerful tool to evaluate fault chronologies. The ${}^{40}\text{Ar}/{}^{39}\text{Ar}$ ages indicate that the island has been volcanically active since at least 1.62 ± 0.030 Ma (2SD). Volcanism deposited lavas over the entire island until ~ 200 ka, when it became focused along an E–W-trending summit vent system; all dated lavas < 200 ka were emplaced on the southern flank. Structural observations suggest that the island has experienced two major faulting episodes. Crosscutting relationships of lavas indicate that north flank faults formed after 1.16 ± 0.070 Ma, but likely before 416 ± 36 ka, whereas the faults on the southern flank of the island initiated between 201 ± 37 and 32.6 ± 4.6 ka, based on ${}^3\text{He}$ exposure dating of fault surfaces. The data are consistent with a model wherein the northeastern faults are associated with regional extension owing to the young volcano's location closer to the Galápagos Spreading Center at the time. The second phase of volcanism is contemporaneous with the formation of the southern faults. The expression of this younger, low-volume volcanic phase was likely related to the elongate island morphology established during earlier deformation. The complex feedback between tectonic and volcanic processes responsible for southward spreading along the southern flank likely generated persistent E–W-oriented magmatic intrusions. The formation of the Galápagos Transform Fault and sea-level fluctuations may be the primary causes of eruptive and deformational episodes on Santa Cruz.

Keywords Basalt · Hotspot · Ocean island · Structure · Volcano

Introduction

Editorial responsibility: W. W. Chadwick, Jr.; Deputy Executive Editor: L. Pioli

This paper constitutes part of a topical collection:

Volcanic processes: tectonics, deformation, geodesy, unrest

✉ D. M. Schwartz
darinschwartz@boisestate.edu

¹ Dept. of Geosciences, Boise State University, Boise, ID, USA

² Dept. of Geology, Colgate University, Hamilton, NY, USA

³ Dept. of Marine Chemistry and Geochemistry, Woods Hole Oceanographic Institute, Woods Hole, MA, USA

⁴ Dept. of Earth and Environment, Franklin and Marshall College, Lancaster, PA, USA

The morphology of a volcanic edifice within any hotspot-generated archipelago is a product of the interplay between constructional volcanic activity and destructive deformational and erosional processes (Ramalho et al. 2013). The balance between these processes changes with time and leads to morphological variations of both seamounts and islands (Ramalho et al. 2013). Faulting on the flanks of ocean island volcanoes signals structural instabilities, poses tectonic hazards to inhabitants (Carracedo 1996), contributes to the architectures of freshwater supplies (d’Ozouville et al. 2008), and can serve as the source of volcanic eruptions (Montgomery-Brown and Miklius 2021). Thus, the presence or absence of faults and fissures reflects both magmatic and tectonic processes of volcanic edifices, providing insight into the evolution of an ocean island system.

The relative magnitudes of internal and external stresses within an ocean island volcano control the likelihood of a volcanic eruption (Gudmundsson 2012), the orientation of magma emplacement (Takada 1994), and the extent and geometry of flank spreading and faulting (Le Corvec and Walter 2009). Internal stresses within a volcanic edifice are induced by magmatic overpressures (Huppert and Woods 2002). At ocean islands, the magnitude of this stress is a result of the buoyancy force of a magma reservoir, which is related to magma density (Pinel and Jaupart 2000) and exsolution of volatiles (Geshi et al. 2020). External stresses are generated by local and regional topography, diminishing as a function of increased magma storage depth. Regionally, the least compressive stresses will be dominated by gravitational extension, which in turn reflects thermal subsidence as a function of increasing distance from the nearest spreading ridge (Neves et al. 2004) and sea-level fluctuations (Luttrell and Sandwell 2010). Locally, stresses are dominated by the load of the volcanic edifice (Pinel and Jaupart 2003). Eruptions will occur either when the internal stress exceeds the least compressive external stress or when that external stress decreases (Gudmundsson 2012). The dominant causal mechanism will be reflected in the relative orientation of structures and occurrence of eruptions, as well as their temporal relationships with tectonic evolution and sea-level fluctuations.

In this contribution, we investigate the dynamic feedback between internal and external stresses on Isla Santa Cruz, a faulted ocean island volcano in the Galápagos Archipelago. Santa Cruz is an older shield volcano in the Galápagos, morphologically distinct from the younger volcanoes in the western archipelago. Enabled by a novel combination of $^{40}\text{Ar}/^{39}\text{Ar}$ lava flow geochronology and ^3He exposure dating of faults, we use the relative ages of faults and lavas to determine the dominant processes responsible for volcanism and deformation during the island's evolution.

Background

The Galápagos is a hotspot-derived volcanic archipelago that rests upon a shallow ESE-trending basaltic platform on the Nazca Plate (Fig. 1; McBirney and Williams 1969). Hotspot volcanism in the Galápagos is commonly attributed to the melting of a mantle plume, sourced in the deep mantle according to seismic tomography (French and Romanowicz 2015). The westernmost island of Fernandina is the most active volcano in the archipelago (Kurz et al. 2014), located at or near the present-day plume center (Hooft et al. 2003; Villagómez et al. 2007, 2014). As the islands are carried

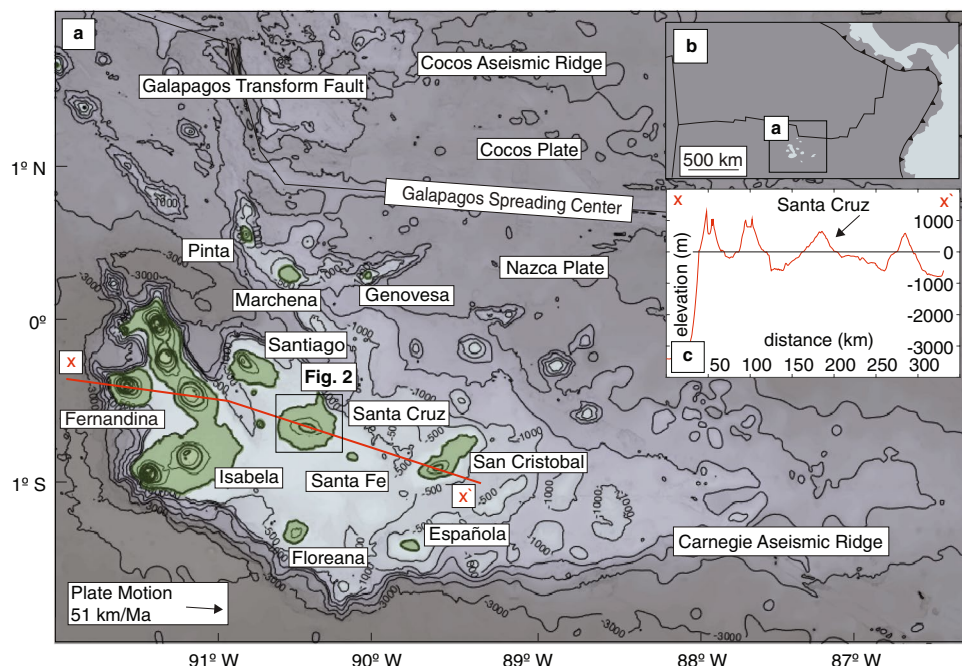


Fig. 1 **a** Map of the Galápagos Archipelago from compiled multi-resolution bathymetric and topographic data (Ryan et al. 2009). Isla Santa Cruz and the location of Fig. 2 are near the center of the archipelago. Index contours are shown as bold lines starting at sea level and at 500 m intervals. Islands are shaded green. Subaerial contour interval is 250 m, and submarine contour interval is 500 m. Absolute plate direction and motion for the Nazca Plate are indicated with the

black arrow and were calculated using Argus et al. (2011). Red line is the trace of an elevation profile from x to x' shown in **c**. **b** Map showing the relative location of the Galápagos Archipelago to Central and South America. Mid-ocean ridges are solid black lines and trenches are toothed lines. **c** Elevation profile across the islands in the central portion of the archipelago

eastward on the Nazca Plate, away from the plume (Fig. 1), magmatism wanes (Ramalho et al. 2013) and they subside (Huppert et al. 2020), resulting in their eventual submergence ~5 Ma after their initial formation (Geist et al. 2014). This lifecycle is modulated by sea-level fluctuations (Schwartz et al. 2018) and the proximity of the mantle plume to the Galápagos Spreading Center (GSC; Harpp and Geist 2018). Migration of the GSC relative to the plume variably partitions magmatism from the Archipelago to the GSC (Cleary et al. 2020), which is manifested as aseismic ridges on the Nazca and Cocos Plates (e.g., Werner et al. 2003; Harpp et al. 2005; Orellana-Rovirosa and Richards 2018; Fig. 1). Plume–ridge distances are also modulated by ridge jumps toward the Galápagos mantle plume over the past 5 Ma (Mittelstaedt et al. 2012).

The morphology of volcanoes along the central hotspot track in the Galápagos varies from west to east (Fig. 1; McBirney and Williams 1969; White et al. 1993). Younger western volcanoes (Fernandina, shields of Isabela) are tall structures (>1500 m; Fig. 1) with summit calderas that erupt lava through radial and circumferential vent systems (Chadwick and Howard 1991). The eastern islands (i.e., Santiago, Santa Cruz, San Cristóbal) are lower relief than the western shields (Fig. 1c), characterized by linear summit vent systems and lacking calderas (Fig. 1a and 1c; Swanson et al. 1974). Gravity surveys on Santa Cruz and San Cristóbal indicate that neither island ever hosted summit calderas, in contrast to the present-day western Galápagos shields (Cleary et al. 2020). This observation suggests that there is no evolutionary relationship between the eastern islands and their younger western counterparts (Harpp and Geist 2018).

Santa Cruz is the most populous island in the Galápagos; most inhabitants (>10,000) live within a graben formed by two of the most prominent faults on the island's southern flank (Fig. 2 and Fig. 3b). Two phases of volcanism, the Platform Series and Shield Series (Bow 1979), define the volcanic stratigraphy of the island. Together, they represent over a million years of activity that extends to nearly the present day (Cox and Dalrymple 1966; Bailey 1976; Bow 1979; White et al. 1993; Kurz and Geist 1999), with the youngest dated volcanism recorded and replicated at 24 ± 11 ka by K/Ar geochronology (White et al. 1993). There is a complex history of submergence and re-emergence of the island recorded as subaerial lavas overlain by marine carbonates in the stratigraphy exposed, now subaerially, on the island's flanks and on minor outlying islands (Bow 1979). This puzzling history of long-duration shallow submergence followed by uplift (Bow 1979) contradicts the prediction of pure subsidence in response to the island's motion away from a mantle plume (Huppert et al. 2020). In this study, we refine the timing of volcanic activity on Santa Cruz and link it to the deformation on the island through direct dating of fault scarps. We test the hypothesis that changes in the dominant

crustal stress fields of the eastern Galápagos volcanoes since their formation can help explain their deformation and uplift history relative to the younger western volcanoes.

Methods

Field observations and mapping

During field work on Santa Cruz, we mapped vents and structural lineaments on the NE and central southern flanks of the island, including faults and fissures, supplemented by previous geologic mapping (Bow 1979). Google Earth satellite imagery and a digital elevation model (d'Ozouville et al. 2008) enhanced identification of structural features elsewhere on the island (e.g., Fig. 2b and c; Fig. 3b), where heavy vegetation limited field access (Fig. 3b).

$^{40}\text{Ar}/^{39}\text{Ar}$ dating

Lava samples for dating by $^{40}\text{Ar}/^{39}\text{Ar}$ geochronology were selected on the basis of geochemical variation to be representative of the island's volcanic history (Wilson et al. 2022). Attention was given to sample localities where ages of lavas could be used to constrain the timing of deformation on the island. Groundmass samples, ~25 mg, <1200 μm , were separated by hand picking from crushed whole rock. These samples were irradiated and analyzed at Oregon State University using an ARGUS VI multi-collector noble gas mass spectrometer following the methods described in Fox et al. (2021). The incremental heating steps creating a plateau in $^{40}\text{Ar}/^{39}\text{Ar}$ were averaged to produce an age for each sample. The reliability of ages was evaluated using the inverse isochron approach, where samples producing negative or discordant ages were discarded (Kuiper 2002; Online Resource 1).

^3He surface exposure dating

Cosmogenic ^3He can be used to quantify the duration of near-surface exposure to cosmic rays, which serves as a mechanism to date volcanic eruptions (e.g., Kurz 1986a; Blard 2021). This approach can be adapted to the direct dating of deformation. To do this, lava samples are collected from fault scarps, where their initial exposure is associated with deformation (Mackey and Quigley 2014; Blahút et al. 2020). In this scenario, the exposure age of a sample reflects the age of a scarp-forming event assuming no erosion and negligible non-cosmogenic ^3He production (Blard 2021). We collected samples for ^3He exposure dating from basaltic lava flows, typically within vertical fissures formed by normal faulting in the subsurface (Martel and Langley 2006). Cosmic rays penetrate rock resulting in ^3He production in

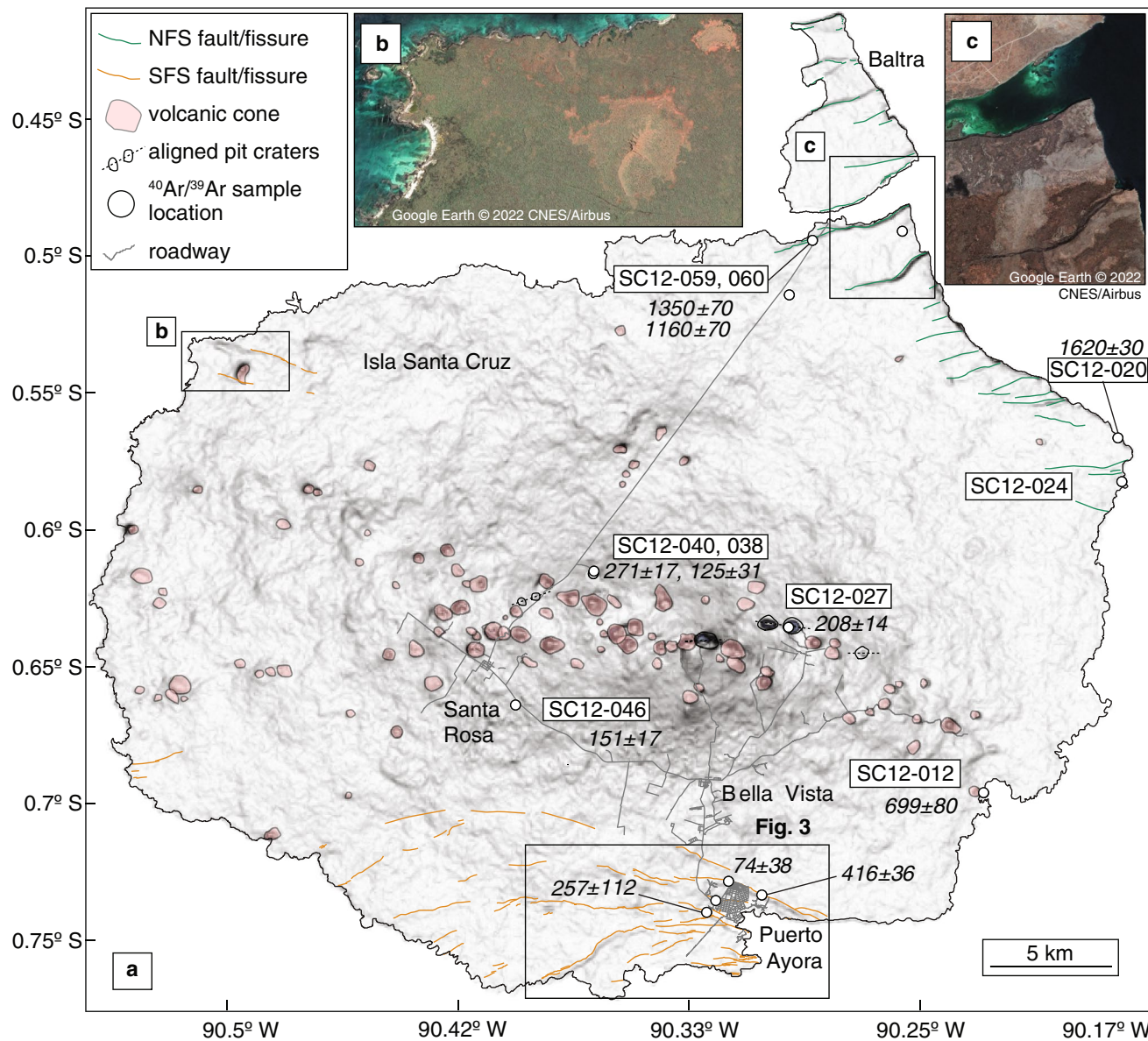


Fig. 2 **a** Map of Baltra and Santa Cruz illustrating prominent structural and volcanic features mapped using satellite data. $^{40}\text{Ar}/^{39}\text{Ar}$ ages (ka) are shown in italics, for those samples whose step heating plateaus are concordant with inverse isochron ages. Details from

the inset are shown in Fig. 3; names for samples in Fig. 3 inset are not included on this map. **b** Satellite image of the faults exposed on the northwestern flank of Santa Cruz. **c** Satellite image of the NFS exposed on the northeastern flank of Santa Cruz

the subsurface, but their effect is attenuated as a function of depth (Dunne et al. 1999). Thus, samples were removed from fissure/fault walls as low in the volcanic stratigraphy as possible to minimize cosmogenic exposure prior to faulting.

Samples were sawed square to a thickness of 2–3 cm and then crushed and sieved. Olivine grains were handpicked using a binocular microscope from the 500–850 μm , non-magnetic sieve fraction, unless otherwise noted. Olivine fractions were analyzed using the helium isotope mass spectrometer (MS2) dedicated to rocks and minerals at Woods Hole Oceanographic Institution, consisting of a custom 90°

magnetic sector and a quadrupole mass spectrometer (Kurz 1986b; Kurz et al. 1996; Kurz and Geist 1999). Measurements were taken by vacuum crushing and melting extractions of each olivine mineral separate. Crushing the sample releases the He contained primarily in melt and fluid inclusions, which is most representative of the inherited component and measured as $^{3}\text{He}/^{4}\text{He}$ (Kurz 1986a). Melting the crushed fraction in a single step releases the remaining gas, yielding total concentrations of ^{3}He and ^{4}He (Kurz 1986a), a combination of the cosmogenic and magmatic helium in the olivine powder. The cosmogenic component of the ^{3}He

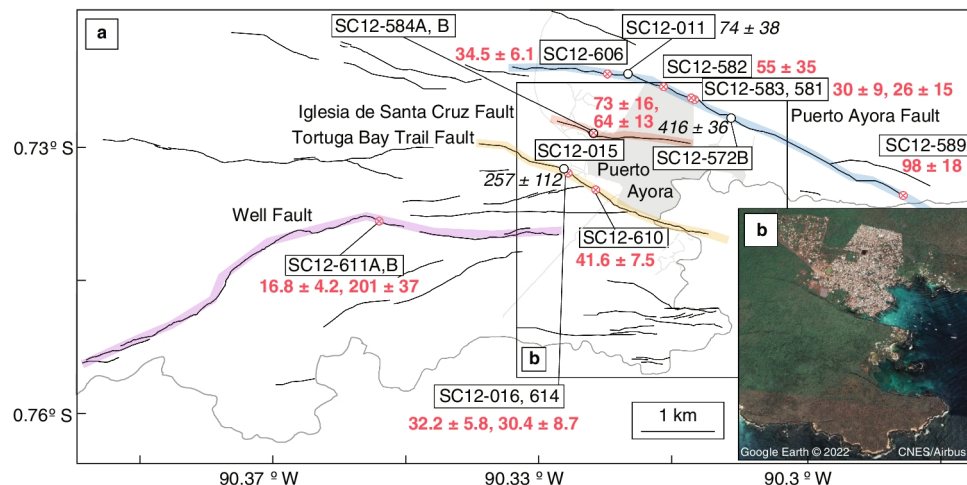


Fig. 3 **a** Map illustrating prominent structural features identified using satellite data and the locations of cosmogenic age samples near the town of Puerto Ayora on the southern flank of Santa Cruz (see Fig. 2 inset). Faults targeted for geochronology are highlighted in pastel colors. Geochronology sample names are shown in boxes. Locations of $^{40}\text{Ar}/^{39}\text{Ar}$ samples are marked as open black circles, ages (ka)

in italic text, and cosmogenic ^3He exposure dating samples as circled red exes, ages (ka) in red text. Faults are represented as curved black lines, and the shoreline is demarcated as a thin grey line. Black box indicates the location of inset **b**. **b** Satellite image of the SFS exposed near the town of Puerto Ayora on the southern flank of Santa Cruz

can be calculated from the two measurements, assuming that the inherited $^3\text{He}/^4\text{He}$ ratio is negligibly affected by cosmogenic ^4He (Kurz 1986b). Radiogenic ^4He ($^4\text{He}^*$) can also affect apparent cosmogenic age (Blard 2021), but for the relatively young samples in this study, $^4\text{He}^*$ is estimated to be less than the error on the $^4\text{He}_{\text{melt}}$ measurement (Online Resource 2) and is negligible. Atmospheric helium adsorption, occurring after crushing and prior to melting, may lead to overcorrection of the magmatic ^3He component by several percent (Protin et al. 2016) to an extent that cannot be quantified, but was minimized by venting to nitrogen following the crushing step.

For exposure age calculations, we used the online exposure age calculator, CREp (Martin et al. 2017). Calculations were performed using a global average sea-level high-latitude ^3He production rate in olivine of 119.03 ± 11.73 at/g/yr (Goehring et al. 2010), scaled to the latitude and elevation of each sample site, based on time-dependent LSD model of geomagnetic fluctuations (Lifton et al. 2014) and the ERA40 atmosphere model (Uppala et al. 2005). All samples were at least partially shielded by topography (Balco et al. 2008) and from cosmic ray attenuation as a function of sample thickness (Dunne et al. 1999). Thus, ages were calculated accounting for attenuation based on the thickness of each sample, an average sample density of 2.7 g/cm^3 and topographic shielding from horizon measurements made at each sample site (Online Resource 3). Although there was additional self-shielding owing to dipping sample surfaces (Balco et al. 2008), we did not include this adjustment because our horizon measurements generally account for this aspect of the sample's geometry (Online Resource 3). Ultimately, shielding-corrected exposure ages were calculated

from each sample's cosmogenic ^3He concentrations divided by the sample-specific production rate. This rate is computed as the product of scaling factors derived from topographic shielding and sample thickness and the reference sea-level production rate. Weighted mean ages are calculated for samples collected ~ 1 km from each other and along the same fault, as they were likely all originally exposed at the same time, except where noted in the Results. The complex geometry of the fault scarp samples, the resultant topographic shielding correction uncertainties, and uncertainty in production rates all likely to contribute more uncertainty to the absolute ^3He exposure age determinations than the analytical uncertainties.

Results

Fault groups and distributions

We divided the structures on Santa Cruz into two categories on the basis of morphology and location on the island (Fig. 2). In general, faults on the northeastern flank of Santa Cruz are poorly preserved and have vertical offsets that increase shoreward (Fig. 2C); these are referred to as the Northern Fault Series (NFS). In contrast, faults in the south-central sector of the island are more intact and have vertical offsets that exhibit no correlation with proximity to the shore; this group is the Southern Fault Series (SFS; Figs. 2, 3). There are additional small sets of faults on the northwest and southwest flanks of Santa Cruz that are distinct from the two primary fault groups. These isolated faults were not visited in the field campaign, but have been included in the SFS (Fig. 2) because they

exhibit similar morphological characteristics to SFS faults according to satellite imagery (Fig. 2b).

The NFS have similar morphology and orientation to faults observed on minor outlying islands near Santa Cruz (e.g., Baltra; Fig. 2). The NFS have a unimodal distribution with a length-weighted mean orientation of 79° (Fig. 4). Characteristically, the NFS separate hanging and footwall blocks by vertical scarps with large piles of rubble at their bases (Fig. 5); in places, only a steep rubble pile separates the footwall and hanging wall surfaces, with no exposed scarp face. The NFS faults occur as both north- and south-facing structures, forming narrow grabens, such as the one separating Santa Cruz and Baltra Island (Canal de Itabaca; Fig. 5).

The SFS (Fig. 2) exhibits a bimodal directional distribution (modes at 80 and 110°), with a length-weighted mean orientation of 88° (Fig. 4). The SFS faults are expressed as vertically offset fissures that breach the upper hinge of narrow monoclinal folds (Fig. 6), similar to those observed in southwest Iceland (Grant and Kattenhorn 2004) and on the Koae fault system in Hawaii (Peacock and Parfitt 2002). The vertical fissures on SFS faults accommodate vertical and horizontal displacements (Fig. 7), suggesting that they are connected to more shallowly dipping normal faults at depth (Martel and Langley 2006). The location of the hanging wall block relative to the footwall alternates north and south of the fissure, indicating that in the subsurface, fault dips are not preferentially oriented (e.g., there are two faults that form a graben bounding Puerto Ayora to its north and south; Fig. 3).

Monogenetic vent and pit crater distributions and characteristics

Monogenetic vents and pit craters identified in satellite imagery are concentrated along the E–W-trending spine of the island (Fig. 2). The primary dispersion axis

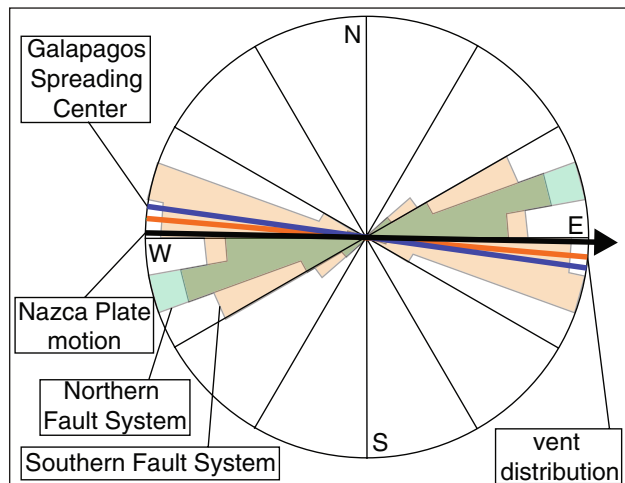


Fig. 4 Rose diagram summarizing the orientation of prominent structural features on Santa Cruz Island relative to regional features

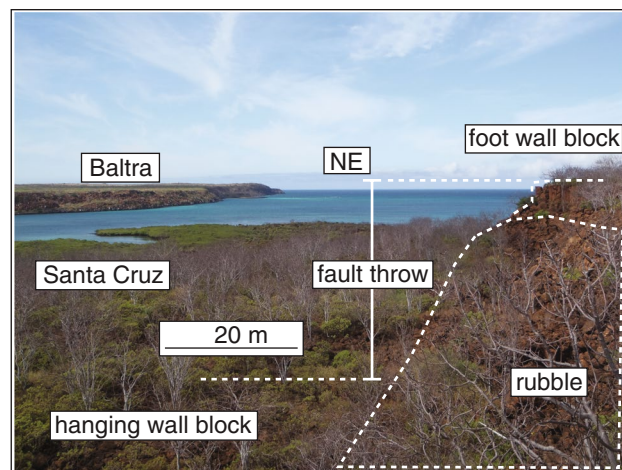


Fig. 5 Annotated handheld photograph, facing Northeast, of a Northern Fault System (NFS) fault at the northeastern-most tip of Santa Cruz. The body of water visible in the background is the channel between Isla Santa Cruz and Baltra

of the volcanic vents is 95° , calculated as the surface-area-weighted directional distribution in ArcGIS (Fig. 4). Pit craters, which are products of subterranean magma evacuation, are elongate and form chains in the direction of magma storage (Wyrick et al. 2004). The mean orientation of pit crater alignments and elongations on Santa Cruz is 86° (Fig. 4).

$^{40}\text{Ar}/^{39}\text{Ar}$ ages of lavas and chronology of volcanism on Isla Santa Cruz

Of the 15 samples collected for $^{40}\text{Ar}/^{39}\text{Ar}$ dating (Online Resource 1), 11 produced plateau ages with concordant (overlapping within uncertainty) inverse isochron ages (Table 1; Figs. 2, 3). Plateau ages from these samples vary from 1.62 ± 0.03 Ma to 74 ± 38 ka (all errors on ages are reported as 2SD). Combined with previous geochronology, the new ages record a history of volcanism on Santa Cruz that spans ~ 1.6 Ma (Table 1), extending active volcanism an additional 300 ka beyond the most recent assessment of the volcano's eruptive history (White et al. 1993). The oldest four ages are from the northeastern flank of Santa Cruz (Figs. 2, 3); these samples are all classified as Platform Series lavas (Wilson et al. 2022). Near the island's summit, samples range in age from 271 ± 14 to 125 ± 31 ka, sampled from pit crater walls as deep within the volcano's stratigraphy as accessible (SC12-027), and from capping lavas and scoria cones. All samples with ages younger than 100 ka are located on the island's southern flank, consistent with previous observations (Cox and Dalrymple 1966; Bow 1979; White et al. 1993; Kurz and Geist 1999).

Several $^{40}\text{Ar}/^{39}\text{Ar}$ dates provide maximum age constraints on the formation of faults for both the SFS and NFS (Fig. 3). The uppermost lava flow on the northeast corner of Santa Cruz (SC12-060; Fig. 2), which was deformed by a fault belonging to the NFS,

Fig. 6 **a** Annotated photograph of the Tortuga Bay Trail Fault, looking southeast toward Puerto Ayora. **b** Annotated photograph of the same fault looking northeast, taken from the Tortuga Bay Trail near the location of **a**

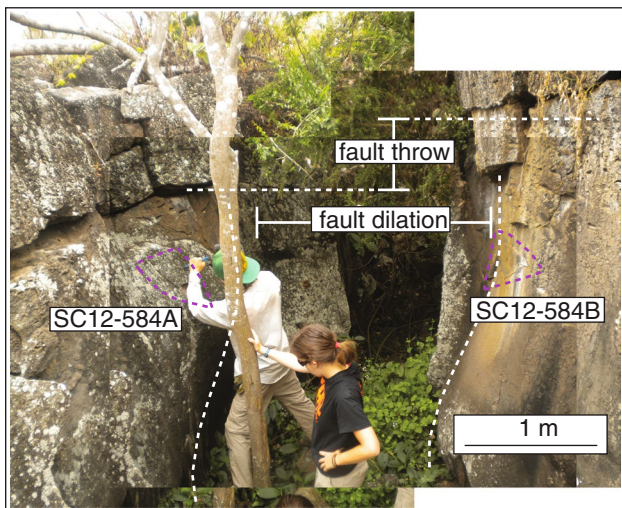
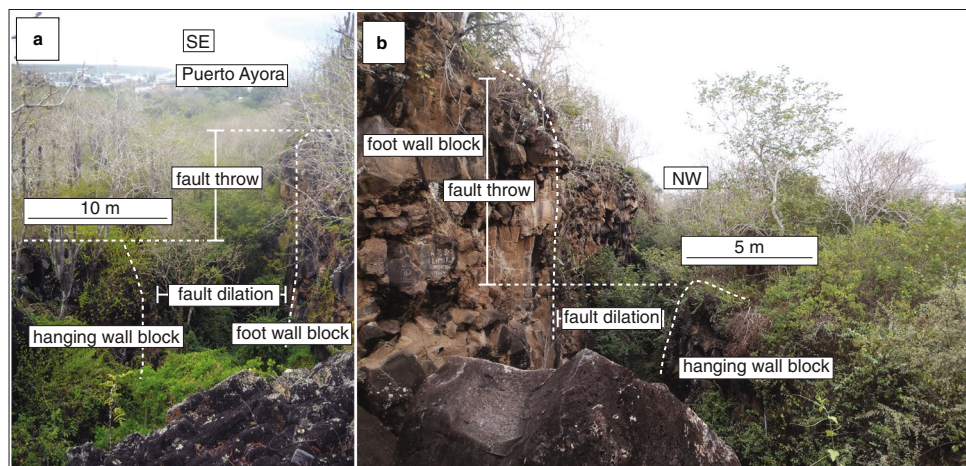


Fig. 7 Annotated mosaic of photographs of the Iglesia de Santa Cruz Fault, part of the SFS, to illustrate the sampling process for cosmogenic ${}^3\text{He}$ samples SC12-584A and SC12-584B. Locations of the samples are shown as dotted purple lines. Van Kirk (foreground) and Schwartz (collecting sample) for scale

yields an age of 1.16 ± 0.07 Ma (Table 1). Sample SC12-572B is the uppermost flow cut by the Puerto Ayora Fault (SFS) and has a plateau age of 416 ± 36 ka. Sample SC12-015, from the highest lava flow on the hanging wall side of the Tortuga Bay Trail Fault, yields an age of 257 ± 112 ka (Figs. 3, 8; Table 1).

Magmatic helium isotopic ratios

The ${}^3\text{He}/{}^4\text{He}$ values obtained upon vacuum crushing of the olivines (6.3 to 8.8 R/R_a; Table 2) are interpreted to represent the magmatic helium. These magmatic values have a mid-ocean ridge basalt-like signature that overlaps but expands the range observed on Santa Cruz (Table 2; Kurz and Geist 1999; 8.58–9.5 R/R_a) and do not support a strong hotspot helium contribution to this magmatism (up

to 30 R/R_a, at Fernandina). The ${}^3\text{He}/{}^4\text{He}$ values obtained upon melting are all significantly greater than the samples' ratios measured on crushing (Table 2; Fig. 8) and are interpreted as a result of cosmogenic production of ${}^3\text{He}$. The ratios are not significantly affected by grain size, alteration, or adhering groundmass, which is confirmed by duplicate analyses (denoted with "fb" appended to the end of sample names in Table 2) of samples from larger (850–1200 μm) and smaller (250–500 μm) size fractions and samples that were mechanically abraded to remove the outer olivine layer, thus removing any potential implanted radiogenic helium (Fig. 8).

Surface exposure ages

Twelve surface-exposure ages were calculated for samples collected along three SFS faults exposed around the town of Puerto Ayora (Fig. 3). The exposure ages (Table 3) are divided into four groups according to the faults from which they were collected (Fig. 9). All samples were at least partially shielded by surrounding topography, with shielding factors varying along each fault and ranging from 0.3 to 0.8 (Table 3). For reference, the average shielding factor of 0.6 nearly doubles the exposure age relative to a hypothetical unshielded sample containing the same amount of cosmogenic ${}^3\text{He}$.

Four samples along the Puerto Ayora Fault were collected from both the hanging and footwall sides of the fault scarp. The ages vary from 26 ± 15 ka to 98 ± 18 ka (all errors on exposure ages are reported as 2SD), with a weighted mean age of 32.6 ± 4.6 ka (Table 3; Fig. 9). There is no clear age progression from east to west along the fault (Fig. 3), and all dates fall within error of one another, with the exception of the oldest sample (SC12-589). The latter was collected from the footwall side of the Puerto Ayora Fault where it meets the ocean, 3–4 km east of the other samples (Fig. 3). Sample SC12-589 is not used in the weighted mean age calculated for this fault, given its distance from the others.

Table 1 Summary of $^{40}\text{Ar}/^{39}\text{Ar}$ eruption ages for Isla Santa Cruz

Sample name	Latitude $^{\circ}$	Longitude $^{\circ}$	Elevation m	Plateau age ka	\pm	$\%^{39}\text{Ar}$	Inverse isochron age ka	\pm	N ^a	$^{40}\text{Ar}/^{36}\text{Ar}_i$	\pm
						2SD		2SD			2SD
Concordant ages											
SC12-011	-0.73148	-90.31692	47	73.6	38	94	83.5	51	11	295.1	5.5
SC12-038	-0.61789	-90.36569	623	125	31	94	69.3	42	14	300.5	3.4
SC12-046	-0.66620	-90.39413	388	151	17	95	180	45	12	289.0	9.8
SC12-027	-0.63759	-90.29519	416	208	14	74	242	35	8	292.3	3.2
SC12-015	-0.74286	-90.32467	41	257	112	95	320	171	15	294.4	3.4
SC12-040	-0.61715	-90.36520	603	271	17	81	282	54	9	294.5	4.7
SC12-572B	-0.73636	-90.30458	38	416	36	98	386	76	12	296.7	2.7
SC12-012	-0.69863	-90.22364	0	699	80	67	594	143	9	296.7	1.5
SC12-060	-0.49394	-90.28582	30	1160	70	58	1470	630	6	290.1	12
SC12-059	-0.49388	-90.28613	28	1350	70	100	1270	70	20	300.3	2.2
SC12-067	-0.49090	-90.25342	48	1360	30	100	1370	40	17	295.2	1.0
SC12-020	-0.56739	-90.17453	36	1620	30	100	1620	40	20	296.4	2.8
Discordant or negative inverse isochron ages											
SC12-059	-0.49388	-90.28613	28	1260	210	66	370	230	12	313.2	20
SC12-024	-0.58360	-90.17330	16	40.1	106	97	-250	112	19	297.4	1.7
SC12-584B	-0.73856	-90.32131	31	900	600	25	-2210	3990	3	305.2	27
SC12-070	-0.51437	-90.29446	72	-3700	660	60	2780	2060	16	290.4	2.3

^a Number of heating steps used in plateau and inverse isochron age calculations

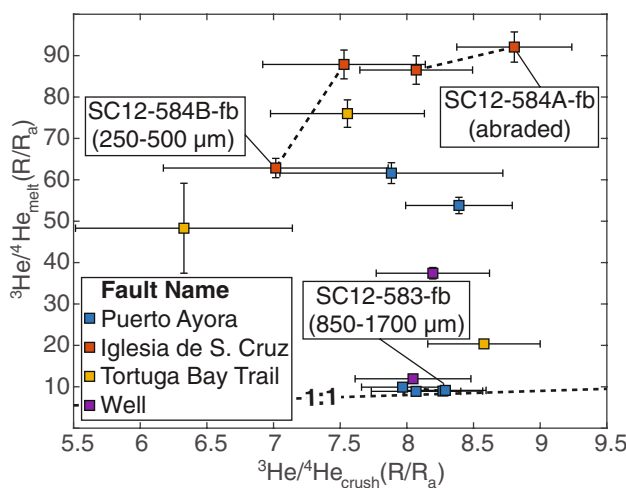


Fig. 8 Helium isotope ratios for crushing and melting experiments performed on cosmogenic dating samples. Error bars are 2SD. Colors of samples correspond to the highlighted faults in Fig. 3. Dashed lines connect different aliquots of the same sample. Equal isotope ratios from crushing and melting would fall along the 1:1 line and would be consistent with zero age, based on the assumption that all melt $^{3}\text{He}/^{4}\text{He}$ above the line is produced by cosmogenic ^{3}He

Three samples were collected from the Tortuga Bay Trail Fault (Fig. 3). Two were from sites adjacent to each other within the same fissure, where one massively jointed lava flow detached

along a cooling joint. The ages of these two samples should, therefore, be identical and represent the same deformation event. The sample from the hanging wall side of the fissure, SC12-016, yielded an exposure age of 32.2 ± 5.8 ka, indistinguishable from the adjacent sample from the footwall side of the fissure (SC12-614: 30.4 ± 5.8 ka; Fig. 8). We collected a third sample (SC12-610) from the same fault less than one kilometer southeast of the other two, which yielded an age of 41.6 ± 7.5 ka (Fig. 8). We calculated a weighted mean age for the Tortuga Bay Trail Fault of 34.6 ± 4.1 ka from these three samples, which is coeval with formation of the North Puerto Ayora Fault.

Two samples from the same lava flow were analyzed for exposure ages from adjacent faces of the same fissure (SC12-584A and 584B; Fig. 7) on the Iglesia de Santa Cruz Fault (Fig. 3). In this location, joint patterns in the basalt could be matched across the fissure (Fig. 7). Therefore, the two samples should share an identical exposure history, which in turn represents the age of the fissure. When corrected for shielding, the two ages are indistinguishable from each other at 73 ± 16 ka and 64 ± 13 ka (Table 3; Fig. 8). The samples have a weighted mean age of 67.7 ± 6.9 ka. The average age of the Iglesia de Santa Cruz Fault is about twice that of the larger faults to its north and south.

Two samples collected from the Well Fault yielded both the youngest and oldest exposure ages of any of the Santa

Table 2 Helium isotope measurements and calculations for ${}^3\text{He}_{\text{cosmo}}$ and are grouped by the fault they were collected from, ordered from west to east

sample name	Sample mass g	${}^4\text{He}_{\text{crush}}$	${}^4\text{He}_{\text{melt}}$ ^a	${}^3\text{He}^b/{}^4\text{He}_{\text{crush}}$	\pm	${}^3\text{He}^c/{}^4\text{He}_{\text{melt}}$	\pm	${}^4\text{He}_{\text{melt}}$ ^d	\pm	${}^3\text{He}_{\text{initial}}$ ^e	\pm	${}^3\text{He}_{\text{cosmo}}$	\pm	${}^3\text{He}_{\text{cosmo}}$	\pm		
	ncc STP	ncc STP	2SD	R/R _a		2SD	R/R _a	2SD	g ₁ ⁻¹	ncc STP	2SD	pcc STP g ₁ ⁻¹	2SD	pcc STP	2SD	atoms g ⁻¹	2SD
Yerueta Ayora Fault																	
SC12-606	0.30911	0.1039	0.2417	0.0048	7.88	0.84	61.61	2.5	0.7820	0.016	0.06668	0.0030	0.008532	0.00092	0.05815	0.0032	8.6×10^4
SC12-582	0.24551	2.316	12.81	0.26	8.07	0.34	8.89	0.30	52.19	1.0	0.6424	0.025	0.5829	0.027	0.05952	0.037	9.8×10^5
SC12-583	0.28876	6.313	5.532	0.11	7.97	0.31	9.91	0.37	19.16	0.38	0.2627	0.011	0.2113	0.0092	0.05143	0.015	3.8×10^5
SC12-583-1b ⁱ	0.13707	18.92	8.262	0.17	8.27	0.30	8.96	0.31	60.28	1.2	0.7476	0.030	0.6899	0.028	0.05770	0.041	1.552×10^6
SC12-581	0.29727	15.18	9.331	0.19	8.29	0.31	9.13	0.34	31.39	0.63	0.3965	0.017	0.3601	0.015	0.03643	0.023	9.796×10^5
SC12-589	0.29002	0.8718	0.9820	0.020	8.39	0.40	53.80	2.0	3.386	0.068	0.2521	0.011	0.3932	0.0020	0.2128	0.011	2.8×10^5
Gleisa de Santa Cruz Fault																	
SC12-584A	0.22261	0.7449	0.2889	0.0058	8.07	0.42	86.52	3.4	1.298	0.026	0.1554	0.0069	0.01449	0.00081	0.1409	0.0070	3.788×10^6
SC12-584A-1b ^j	0.24143	1.183	0.2880	0.0058	8.81	0.43	92.07	3.6	1.193	0.024	0.1520	0.0067	0.01454	0.00077	0.1375	0.0068	3.696×10^6
SC12-584B	0.22268	0.2183	0.2143	0.0043	7.53	0.61	87.87	3.5	0.9624	0.019	0.1170	0.0052	0.01003	0.00084	0.1070	0.0053	2.877×10^6
SC12-584B-1b ^k	0.26320	0.07664	0.3647	0.0073	7.02	0.84	62.85	2.3	1.386	0.028	0.1205	0.0051	0.01346	0.0016	0.1071	0.0053	1.4×10^4
Portuga Bay Trail Fault																	
SC12-016'	0.18772	0.2863	0.1242	0.0025	7.55	0.58	75.99	3.3	0.6618	0.013	0.06961	0.0033	0.06920	0.00055	0.06269	0.0034	9.0×10^4
SC12-614	0.15547	0.1060	0.09216	0.0018	6.33	0.81	48.31	11	0.5928	0.012	0.03963	0.0090	0.005191	0.00068	0.03444	0.0090	9.260×10^5
SC12-610	0.20176	1.097	1.097	0.022	8.58	0.42	20.36	0.78	5.440	0.11	0.1533	0.0066	0.06458	0.0034	0.08870	0.0075	2.385×10^6
Vell Fault																	
SC12-611B	0.22050	0.71891	0.8714	0.017	8.20	0.43	37.43	1.4	3.952	0.079	0.2047	0.0086	0.04482	0.0025	0.1599	0.0090	4.300×10^6
SC12-611AC ^j	0.25705	0.59336	1.004	0.020	8.05	0.43	11.93	0.51	3.904	0.078	0.06445	0.0031	0.04347	0.0025	0.02097	0.0039	5.639×10^5

He measured on the lung assuming 2% error on each measurement

${}^3\text{He}/{}^4\text{He}$ measured on crushing (R) reported relative to the atmospheric ${}^3\text{He}/{}^4\text{He}$ ($R_\infty = 0.000001384$)

MEASUREMENT CRUSHING 11

$^{32}\text{He}/^{34}\text{He}$ measured on

${}^4\text{He}_{\text{melt}} / {}^3\text{He}_{\text{melt}}$ sample mass $\times {}^4\text{He}_{\text{melt}} \times \text{R}_a$

$^3\text{He}/^4\text{He}_{\text{crush}} \times ^4\text{He}_{\text{melt}} \times R_a$ (Kun)

${}^3\text{He}_{\text{total}} - {}^3\text{He}_{\text{initial}}$ (Kurz 1986b)

calculated using the ideal gas

850–1700 μm sieve fraction

abraded

250 *Environ Biol Fish*

230–300 μ m sieve fraction

Table 3 Inputs for cosmogenic ^3He exposure age calculation and ages (numbers in bold are weighted mean ages calculated for each fault segment, see [Results](#) for details), organized as in Table 2

Sample name	Latitude	Longitude	Elevation	Production rate scaling factor ^a	Sample thickness	Topographic shielding factor ^b	Shielding corrected exposure age ^c	±
	°	°	m		cm		ka	2SD
Puerto Ayora Fault								
SC12-606	−0.73129	−90.320	49.50	0.64	2.0	0.6032	32.6	4.6
SC12-582	−0.73267	−90.313	24.00	0.65	2.2	0.3820	55	35
SC12-583	−0.73421	−90.309	32.60	0.62	2.0	0.6457	29.5	8.9
SC12-583-fb	−0.73421	−90.309	32.60	0.63	2.0	0.6457	33	21
SC12-581	−0.73431	−90.309	27.10	0.61	2.7	0.5419	26	15
SC12-589	−0.74602	−90.284	22.90	0.65	3.0	0.7744	98	18
Iglesia de Santa Cruz Fault								
SC12-584A	−0.73858	−90.321	20.60	0.65	2.0	0.6817	73	16
SC12-584A-fb	−0.73858	−90.321	20.60	0.65	2.0	0.6817	71	15
SC12-584B	−0.73858	−90.321	20.60	0.65	2.0	0.5878	64	13
SC12-584B-fb	−0.73858	−90.321	20.60	0.65	2.0	0.5878	64	13
Tortuga Bay Trail Fault								
SC12-016	−0.74324	−90.324	25.80	0.62	2.0	0.7176	32.2	5.8
SC12-614	−0.74324	−90.324	25.80	0.62	2.0	0.4211	30.4	8.7
SC12-610	−0.74544	−90.321	29.00	0.66	2.0	0.7468	41.6	7.5
Well Fault								
SC12-611A-C	−0.74902	−90.348	25.00	0.57	2.0	0.5066	16.8	4.2
SC12-611B	−0.74902	−90.348	25.00	0.67	2.0	0.2731	201	37

^a calculated from latitude, longitude and elevation using CREp online calculator (Martin et al. 2017)

^b calculated from Balco et al. (2008) using topographic shielding measurements from Online Resource 3

^c calculated using CREp online calculator using topographic shielding factor, scaled production rate and $^3\text{He}_{\text{cosmo}}$ (Table 2)

Cruz faults, at 16.8 ± 4.2 ka and 201 ± 37 ka (Fig. 9). The samples were located on opposing sides of a fissure less than 10 m apart (Fig. 10). Given the disparity between the ages, a weighted mean age was not calculated for this fault. The younger of the samples, SC12-611A, was collected from the footwall of the Well Fault's fissure an estimated 15 m from the top of the footwall, and the older sample (SC12-611B) was collected from 1–2 m from the top of the hanging wall (Fig. 10). Thus, the age relationship between the two samples cannot be reconciled by progressive fault slip. In this case, we interpret the young age of this sample to be the result of recent erosion of the fissure wall, not the original faulting event. Instead, the older age of SC12-611B at 201 ± 37 ka is considered to best represent the formation date of the Well Fault in this location; it is also the oldest exposure age recorded for faulting on the island's southern flank.

Chronology of deformation on Isla Santa Cruz

On the basis of crosscutting relationships, the $^{40}\text{Ar}/^{39}\text{Ar}$ ages indicate that the NFS was active after 1160 ± 70 ka (Fig. 3). No samples were collected from the NFS with enough fresh

olivine for exposure dating. Indirect evidence, however, indicates that the NFS is older than the SFS. First, there are lavas that flow around existing NFS scarps (e.g., Bow 1979), which provide a lower age boundary to the faults. One of these lavas was dated by Ar–Ar methods (SC12-024, Fig. 2), but yielded an unreliable plateau age (Table 1). On the basis of field observations of weathering, NFS scarps appear older than the SFS. Given that the northern flank of Santa Cruz is more arid (~ 50 mm/yr rainfall) than the heavily vegetated southern flank (~ 400 mm/yr; Grant and Boag 1980; Fig. 6), erosion rates are likely slower in the north than in the south. Nevertheless, the SFS are better preserved than the NFS (Figs. 5 and 6), with the majority of the NFS reduced to rubbly slopes (Fig. 5). Thus, we conclude that the NFS were formed during or after Platform Series volcanism, but before the maximum age recorded by SFS-cut lavas at 416 ± 36 ka.

The ^3He exposure ages on the SFS faults overlap the $^{40}\text{Ar}/^{39}\text{Ar}$ ages and corroborate the finding that deformation by the SFS occurred after 416 ± 36 ka, as indicated by the oldest dated lava crosscut by the Well Fault in the SFS (Fig. 3). Synchronous $^{40}\text{Ar}/^{39}\text{Ar}$ and exposure ages, however, make it clear that deformation and faulting on the southern flank were contemporaneous (overlapping

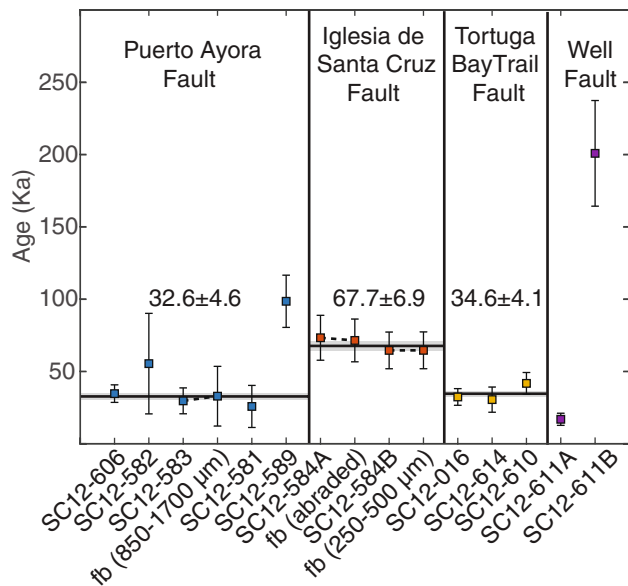


Fig. 9 Cosmogenic ${}^3\text{He}$ exposure ages for 12 samples collected from vertical fault scarps along four of the primary faults on the southern flank of Santa Cruz (Fig. 4). Samples that were collected from the same fault are grouped together and arranged from west to east along strike of the fault from which they were collected. Squares are ages corrected for topographic and geometric shielding with corresponding error bars that include both analytical and production rate uncertainty (2SD). Replicate analyses made on different aliquots (labeled as “fb”) of the same sample are connected with a dashed line. Weighted mean ages are calculated for each fault (except the Well Fault, see [Results](#) for explanation) and represented as horizontal black bars, with uncertainty for the weighted mean age shown as a lighter grey box (Table 3)

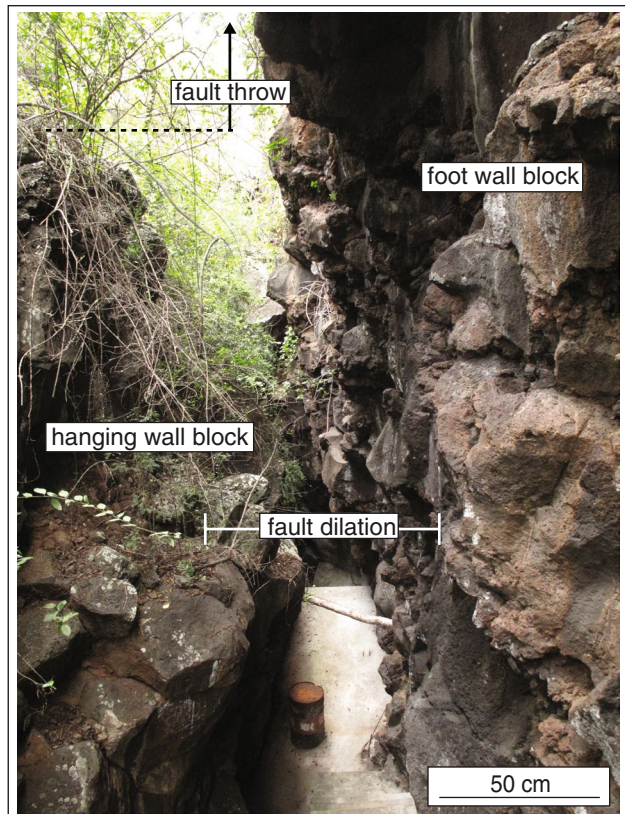


Fig. 10 Annotated photograph of the Well Fault near the sampling location for SC12-610A, from the foot wall block of the fissure and SC12-610B from the hanging wall block, both collected ~1 m from ground level (i.e., the concrete footpath)

probability density function peaks; Fig. 11a). The exposure ages indicate that faulting began at the eastern and western extents of the SFS, where the oldest samples were collected (98–201 ka; Figs. 3, 9). The youngest fault segments (Puerto Ayora Fault and the Tortuga Bay Trail Fault; Fig. 3) have identical weighted mean ages (~35 ka; Fig. 9), providing a constraint on the age of the graben at Puerto Ayora. The graben formed contemporaneously with the youngest dated volcanism on the island, 24 ± 11 ka (White et al. 1993).

Discussion

Tectonic controls on the origins of the NFS and platform series volcanism

The presence or absence of extensional deformation on a volcanic edifice can provide insight into ongoing magmatic or tectonic processes; fault kinematics as well as spatial and temporal relationships between volcanic and structural features can also be used to infer origins of those deformational features. On Santa Cruz, the NFS vertical offsets

increase toward the shoreline (Figs. 2, 3). Assuming a fault’s displacement is centered at its initiation point (e.g., Waterson 1986), the NFS must have begun propagating at or beyond the island’s coastline. Moreover, the NFS orientations are parallel to structures on minor outlying islands, such as Santa Fe, located southeast of Santa Cruz (Fig. 1; Bow 1979). Consequently, we conclude that the stress field responsible for the formation of the NFS was probably regional, and not controlled by gravitational forces associated with edifice topography alone.

Given the present-day half-spreading rate of the GSC (i.e., motion of the Nazca Plate relative to the GSC; ~25 m/ka; Argus et al. 2011), Santa Cruz was 25–50 km closer to the GSC between its emergence (2.3 Ma; Geist et al. 2014) and the end of most Platform Series volcanism (1.16 ± 0.070 Ma; Wilson et al. 2022). The minimum compressive stress for a mid-ocean ridge is predicted to be orthogonal to the strike of the ridge, which is greatest near the spreading center and decreases as a function of distance from the ridge (Neves et al. 2004). The mean orientation of the NFS (79°) is similar to but less than the average strike of the GSC (95° ; Fig. 4) and consistent with

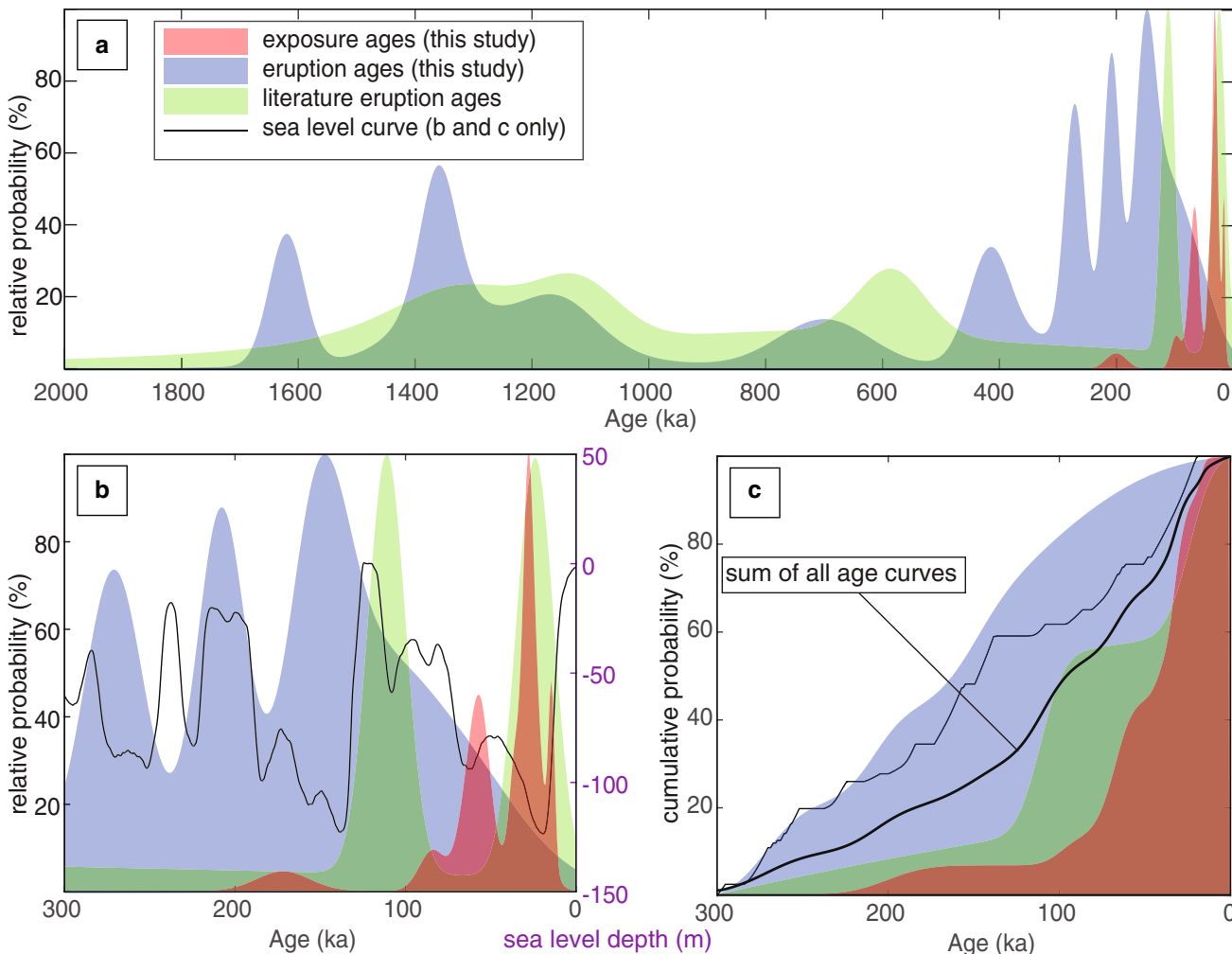


Fig. 11 **a** Summary of geochronological results shown as probability density functions for exposure ages of fault scarps and eruption ages determined by $^{40}\text{Ar}/^{39}\text{Ar}$ (this study) and eruption ages from previous studies, including ^3He exposure (Kurz and Geist 1999) and K/Ar geochronology (Cox and Dalrymple 1966; Bailey 1976; Bow

1979; White et al. 1993). **b** Summary of geochronological results from **a** compared to the sea level curve for the past 300 ka (Bintanja et al. 2005; see text for details). **c** Cumulative density functions from curves in **b**. Sea-level curve represents the cumulative sea-level decrease over the last 300 ka

the location of Santa Cruz on the western edge of a projection of a right-stepping “locked-transform” fault, along strike of the GSC (Neves et al. 2004). Multiple southward jumps of the eastern segment of the GSC between 1.0 and 2.5 Ma (Mittelstaedt et al. 2012) that extended the transform fault could have generated or enhanced the “locked-transform” stress field, required to generate faults that are not simply orthogonal to the ridge itself (Fig. 4). Thus, regional extension that caused NFS faulting likely reflects the influence of the proximal GSC on Santa Cruz during the spreading center’s reconfiguration. Furthermore, crustal and lithospheric thinning from regional extension may have caused isostatic rebound that resulted in uplift (Weissel and Karner 1989), which is required to explain the subaerial exposure of marine carbonates on sea-cliff sections, tens of meters above the sea surface today (Bow

1979). An alternative explanation is that relatively fast sea-level rise since the last glacial maximum has outpaced subsidence related to isostatic compensation.

Alternative explanations for faulting observed in eastern Galápagos islands have been proposed, or are possible. Swanson et al. (1974) invoked upward flexure of the Galápagos Platform in response to a buoyant mantle plume (Huppert et al. 2020) as an explanation for regional extension that generated both faulting and uplift across the central Galápagos; they suggested that the mantle plume defined an east–west-oriented sheet spanning the width of the archipelago. Recent seismic tomography (Villagómez et al. 2014), however, indicates that elevated mantle temperatures associated with the Galápagos plume define a vertical cylinder restricted to the western archipelago, making upward flexure of the lithosphere an unlikely cause of NFS deformation.

Another possibility is that the faults are the result of gravitational spreading of the margins of the Galápagos platform (McGuire 1996). The lack of clearly defined faults on islands in the central archipelago that emerged after the cessation of NFS faulting ~ 1 Ma (e.g., Santiago; Gibson et al. 2012; Floreana; Harpp et al. 2014) suggests that regional deformation had ceased prior to the emergence of these islands. Gravitational spreading of the platform, by contrast, should be an ongoing process, even today. Therefore, we conclude that the geochronology data presented here are most consistent with a model in which regional extension and uplift of the older Galápagos islands are related to Santa Cruz's proximity to the GSC and its tectonic reconfigurations between 1 and 2.5 Ma.

Topographic controls on the formation of the SFS and shield series volcanism

The SFS defines a bimodal (Fig. 4), concave-outward distribution, with faults trending northeast on the southwestern flank but northwest on the southeastern flank (Fig. 2). These geometries are consistent with formation in a topographically dominated stress regime (Dieterich 1988). Gravitational extension alone, however, is not sufficient to cause such deformation, because Santa Cruz's flank slopes ($3\text{--}4^\circ$; Fig. 1) are shallower than the angle of repose, even for unconsolidated cinder cones (20° ; Porter 1972). An alternative explanation is that faults are formed in response to magmatism, similar to continental rifts (Medynski et al. 2016), given the nearly synchronous record of the initiation and cessation of summit and southern flank volcanism (271 ± 17 ka this study to 24 ± 11 ka White et al. 1993) and fault formation (201 ± 37 ka to 32.6 ± 4.6 ka (Fig. 11b and c).

Graben formation in volcanic settings is a common consequence of shallow dike emplacement (e.g., Rubin 1992; Trippanera et al. 2015; Ruch et al. 2016). Thus, the presence of grabens in both the NFS (Fig. 5) and SFS (Fig. 3) may be evidence that deformation was driven by volcanism during both faulting events. We propose that the faults formed in response to persistent E-W-diking events that exploited the local stress regime generated by the existing E-W elongate volcanic edifice, which in turn is a result of the older NFS deformation.

There was a broad migration of volcanism during the Shield Series (Wilson et al. 2022) coincident with the timing of SFS deformation. Lava flows were emplaced on both the northern and southern flanks of the island until 220 ka (White et al. 1993; Kurz and Geist 1999; this study). Volcanism was focused along the E-W-trending summit vent system by 271 ± 17 ka and continued there until at least 125 ± 31 ka (Fig. 2). The beginning of this interval coincides approximately with the two oldest exposure ages of the SFS, 201 ± 37 and 98 ± 18 ka (Fig. 11b). Samples younger than 220 ka are concentrated exclusively on or south of the summit vents (Fig. 2; Kurz and Geist 1999; White et al.

1993; Figs. 2, 3), indicating that by 220 ka, volcanism on the island was migrating south of the summit, directing lava flows onto the southern flank until 24 ± 11 ka (White et al. 1993). This timing of eruptive activity coincides with the youngest exposure ages of faulting (e.g., 32.6 ± 4.6 ; Fig. 9). The reorientation of eruptive features toward an unstable island flank has been observed at other volcanoes, including Hawaii (Le Corvec and Walter 2009) and the Canary Islands (Walter et al. 2005), and is consistent with our observations at Santa Cruz. Consequently, we suggest that a feedback loop was established between persistent east–west-oriented dike intrusions and flank instability, leading to the southward migration of Shield Series volcanism and SFS formation.

External causes of volcanism at Isla Santa Cruz

At Santa Cruz, contemporaneous $^{40}\text{Ar}/^{39}\text{Ar}$ and ^3He exposure ages corroborate a link between deformation and volcanism, at least during the formation of the SFS. Unlike the western Galápagos today, however, there is no evidence that the stress field during the formation of either the NFS or SFS was dominated by periodic overpressure cycles associated with magma recharge (Huppert and Woods 2002; Chadwick and Dieterich 1995). In the presence of shallow magma reservoirs, magmatic overpressure generates radial or circumferential features expressed as directional distribution of vents and structures, which are not observed on Santa Cruz (Fig. 4; Chadwick and Howard 1991). Therefore, we suggest that Santa Cruz has never hosted a long-lived, shallow magma reservoir. This interpretation is consistent with relatively primitive and variable lava compositions, of all ages, on Santa Cruz that indicate a persistent absence of a thermochemically buffered, magma storage reservoir (Wilson et al. 2022). In addition, gravity measurements on Santa Cruz do not record the same positive Bouguer anomalies that are observed in the western archipelago that are predicted to result from the formation of dense-cumulates, generated during periods of shallow magma storage (Cleary et al. 2020). By contrast, we have shown that deformation and volcanism exploited linear, E–W-trending regional or gravitational stress regimes during Shield Series volcanism and the formation of the NFS and SFS (Figs. 2 and 4). Given that the ages of these fault systems span nearly the entire duration of exposed volcanism on the island, we suggest that the orientation of magma emplacement has been controlled primarily by the existing external stress field.

The lack of a magmatically dominated stress regime (i.e., radial or circumferential faulting) during volcanism and deformation on Santa Cruz could be the result of a consistently lower magma supply to the island than is the case for the western volcanoes today. A decreased magma supply would prevent formation of a shallow, steady-state magma reservoir required to impart a radial stress field during

volcanism. Santa Cruz likely had a reduced magma supply early in its construction owing to the island's proximity to the GSC (Wilson and Hey 1995; Mittelstaedt et al. 2012; Cleary et al. 2020); by contrast, the younger Galápagos volcanoes, which formed at a greater plume–ridge distance, likely have a more robust magma flux (Harpp and Geist 2018). A proximal ridge siphons plume material toward its axis, as exhibited by many geochemical and geophysical studies that document migration of plume material to nearby spreading centers (Detrick et al. 2002).

More recently, Santa Cruz's low magma supply is the result of increased distance of the island from the center of the plume (Fig. 1). Unlike the western Galápagos volcanoes, where eruptions are caused primarily by magma overpressures (Vigouroux et al. 2008; Bell et al. 2021) or triggered by seismic events (Gregg et al. 2018), we suggest that in the eastern Galápagos, the relatively low-volume melts are stored until there are changes in the least-compressive stress regime, such as extension related to the reconfiguration of the GSC during Platform Series volcanism.

An additional driver of volcanic activity at Santa Cruz may be sea-level changes (McGuire et al. 1997). There is a rough correlation between the timing of recent volcanism and sea-level regressions at Santa Cruz (Fig. 11b). During times when sea level dropped significantly, particularly during the regressions leading up to the last two largest glacial maxima ~150 ka and 20 ka (Bintanja et al. 2005), there is an increase in the number of eruption and deformation-related exposure ages (Fig. 11b). The most recent glacial maximum at ~20 ka also broadly coincides with the youngest recorded deformation and volcanic events on Santa Cruz (Tables 1 and 2). This relationship is further supported by the synchronous increase in slope of the cumulative probability density functions for eruption ages and exposure ages when compared to the curve for cumulative sea level fall at ~50 ka (Fig. 11c). Furthermore, the summed cumulative density functions for all eruptive ages closely resemble the shape of the curve for cumulative sea-level fall (Fig. 11c). The influence of sea-level change on volcanism also explains the lack of eruption- and deformation-related exposure ages recorded since the last glacial maximum and subsequent transgression (Figs. 10b and c). Consequently, we suggest that during regressions when sea level drops by at least 100 m, there may be sufficient decompression to trigger diking events that lead to flank deformation and eruptions. Additionally, undercutting of the island's flanks during sea-level low stands (Ramalho et al. 2013), as evidenced by steep erosional cliffs on the island's flanks, may lead to their oversteepening and subsequent gravitational collapse, further enhancing magma emplacement and volcanism. The relationship between the timing of sea-level regression and volcanism has been recognized in other low-magma flux ocean island systems such as the Canary (Lietz and Schmincke 1975) and Cape Verde

Islands (Samrock et al. 2019) and may be linked to Pleistocene volcanism in the Azores (Ramalho et al. 2020). Like Santa Cruz, other ocean island volcanoes derived from low buoyancy flux hotspots or near-ridge plumes may be especially susceptible to changes in external stress as a trigger for volcanism and deformation.

Conclusions

Through the application of $^{40}\text{Ar}/^{39}\text{Ar}$ dating of lavas and ^3He exposure ages of fault scarps, we have shown that there were two linked phases of deformation and volcanism on Isla Santa Cruz. Initial deformation is recorded on a fault system exposed on the northeastern flank of the island that occurred contemporaneously with an early phase of volcanism between 1.14 Ma and 420 ka, exploiting a regional stress field associated with the formation and extension of the Galápagos Transform Fault. More recently, deformation on the island's southern flank occurred during (< 225 ka) and until the end of (~35 ka) a second phase of volcanism. Throughout this protracted history of volcanism and deformation, the island experienced a relatively low magma flux compared to the younger western shield volcanoes in the archipelago, reflecting the island's proximity to the Galápagos Spreading Center early in its formation. Given this lower magma flux, the island's morphology and evolution has been dominated by external stresses, as opposed to the periodic overpressure cycles associated with magma recharge that governs the formation of the western volcanoes today. To this end, the timing of volcanic eruptions and deformation are dictated by changes in tectonic stresses at nearby mid-ocean ridges, reconfigurations of those tectonic boundaries, and/or changes in stress associated with unloading during sea-level regressions. The timing of volcanism and deformation at Santa Cruz indicates that a feedback loop can be established between these two processes and that the initial magnitude and changes in the rate of magma supply are a primary control on the evolution of an ocean island.

Supplementary Information The online version contains supplementary material available at <https://doi.org/10.1007/s00445-022-01575-3>.

Acknowledgements We would like to acknowledge the Galápagos National Park for permission to map and collect rock samples (PC-44-15) on Isla Santa Cruz. In addition, we thank colleagues at the Charles Darwin Research Station for facilitating research in the archipelago. We are also grateful to the following individuals for their assistance. Noémie D'Ozouville provided assistance in the field as well as photographs and topographic data used in interpretations for this study. Jillian Schleicher assisted with fieldwork, geochemical analyses, and sample processing. Josh Curtice conducted the He isotope measurements in the Noble Gas Geochemistry Lab at Woods Hole Oceanographic Institution. Dan Miggins and Anthony Koppers performed the $^{40}\text{Ar}/^{39}\text{Ar}$ analyses and helped with their interpretation in the Argon Geochronology Laboratory at Oregon State University, under the direction of Robert Duncan.

We thank Bill Phillips, James Muirhead, Matt Pendleton, Eric Mittelstaedt, and Simon Kattenhorn for early discussions related to this project, reviewers for their thoughtful feedback on this manuscript and William Chadwick for editorial handling. This work was funded by NSF grants EAR-1347731 and OCE-0926491 to K. Harpp. The Noble Gas Geochemistry Lab at Woods Hole Oceanographic Institution is funded by NSF grants from OCE, and OPP-2048351.

Open Access This article is licensed under a Creative Commons Attribution 4.0 International License, which permits use, sharing, adaptation, distribution and reproduction in any medium or format, as long as you give appropriate credit to the original author(s) and the source, provide a link to the Creative Commons licence, and indicate if changes were made. The images or other third party material in this article are included in the article's Creative Commons licence, unless indicated otherwise in a credit line to the material. If material is not included in the article's Creative Commons licence and your intended use is not permitted by statutory regulation or exceeds the permitted use, you will need to obtain permission directly from the copyright holder. To view a copy of this licence, visit <http://creativecommons.org/licenses/by/4.0/>.

References

Argus DF, Gordon RG, DeMets C (2011) Geologically current motion of 56 plates relative to the no-net-rotation reference frame. *Geochem Geophys Geosyst* 12:1–13. <https://doi.org/10.1029/2011GC003751>

Bailey K (1976) Potassium-argon ages from the Galápagos Islands. *Science* 192:465–467. <https://doi.org/10.1126/science.192.4238.465>

Balco G, Stone JO, Lifton NA, Dunai TJ (2008) A complete and easily accessible means of calculating surface exposure ages or erosion rates from ^{10}Be and ^{26}Al measurements. *Quaternary Geochron* 3:174–195. <https://doi.org/10.1016/j.quageo.2007.12.001>

Bell AF, Hernandez S, La Femina PC, Ruiz MC (2021) Uplift and seismicity driven by magmatic inflation at Sierra Negra Volcano, Galápagos Islands. *J Geophys Res Solid Earth* 126:1–18. <https://doi.org/10.1029/2021JB022244>

Bintanja R, van de Wal RSW, Oerlemans J (2005) Modelled atmospheric temperatures and global sea levels over the past million years. *Nature* 437:125–128. <https://doi.org/10.1038/nature03975>

Blahut J, Mitrovic-Woodell I, Baroñ I, René M, Rowberry M, Blard P-H, Hartvich F, Balek J, Meletlidis S (2020) Volcanic edifice slip events recorded on the fault plane of the San Andrés Landslide, El Hierro, Canary Islands. *Tectonophysics* 776:228317. <https://doi.org/10.1016/j.tecto.2019.228317>

Blard P-H (2021) Cosmogenic ^3He in terrestrial rocks: A review. *Chem Geol* 586:120543. <https://doi.org/10.1016/j.chemgeo.2021.120543>

Bow CS (1979) The Geology And Petrogenesis of the lavas of Floreana and Santa Cruz Islands: Galapagos Archipelago. Dissertation, University of Oregon

Carracedo JC (1996) A simple model for the genesis of large gravitational landslide hazards in the Canary Islands. *Geol Soc London Spec Pubs* 110:125–135. <https://doi.org/10.1144/GSL.SP.1996.110.01.10>

Chadwick WW Jr, Dieterich JH (1995) Mechanical modeling of circumferential and radial dike intrusion on Galapagos volcanoes. *J Volc Geotherm Res* 66:37–52. [https://doi.org/10.1016/0377-0273\(94\)00060-T](https://doi.org/10.1016/0377-0273(94)00060-T)

Chadwick WW, Howard KA (1991) The pattern of circumferential and radial eruptive fissures on the volcanoes of Fernandina and Isabela islands, Galapagos. *Bull Volc* 53:259–275. <https://doi.org/10.1007/BF00414523>

Cleary Z, Schwartz DM, Mittelstaedt E, Harpp K (2020) Dynamic magma storage at near-ridge hot spots: Evidence from new Galápagos gravity data. *Geochem Geophys Geosyst* 21:1–15. <https://doi.org/10.1029/2019GC008722>

Cox A, Dalrymple GB (1966) Palaeomagnetism and potassium-argon ages of some volcanic rocks from the Galapagos Islands. *Nature* 209:776–777. <https://doi.org/10.1038/209776a0>

d’Ozouville N, Deffontaines B, Benveniste J, Wegmüller U, Volette S, de Marsily G (2008) DEM generation using ASAR (ENVISAT) for addressing the lack of freshwater ecosystems management, Santa Cruz Island, Galapagos. *Remote Sens Env* 112:4131–4147. <https://doi.org/10.1016/j.rse.2008.02.017>

Detrick R, Sinton J, Ito G et al (2002) Correlated geophysical, geochemical, and volcanological manifestations of plume-ridge interaction along the Galápagos Spreading Center. *Geochem Geophys Geosyst* 3:1–14. <https://doi.org/10.1029/2002GC000350>

Dieterich JH (1988) Growth and persistence of Hawaiian volcanic rift zones. *J Geophys Res Solid Earth* 93:4258–4270. <https://doi.org/10.1029/JB093B05p04258>

Dunne J, Elmore D, Muzikar P (1999) Scaling factors for the rates of production of cosmogenic nuclides for geometric shielding and attenuation at depth on sloped surfaces. *Geomorph* 27:3–11. [https://doi.org/10.1016/S0169-555X\(98\)00086-5](https://doi.org/10.1016/S0169-555X(98)00086-5)

Fox JM, McPhie J, Carey RJ, Jourdan F, Miggins DP (2021) Construction of an intraplate island volcano: The volcanic history of Heard Island. *Bull Volc* 83:1–21. <https://doi.org/10.1007/s00445-021-01452-5>

French SW, Romanowicz B (2015) Broad plumes rooted at the base of the Earth’s mantle beneath major hotspots. *Nature* 525:95–99. <https://doi.org/10.1038/nature14876>

Geist DJ, Snell H, Snell H, Goddard C, Kurz MD (2014) A Paleogeographic Model of the Galápagos Islands and Biogeographical and Evolutionary Implications. In: Harpp K, Mittelstaedt E, d’Ozouville N, Graham DW (eds) The Galápagos: A Natural Laboratory for the Earth Sciences, Geophysical Monograph Series 204 pp 145–166. <https://doi.org/10.1002/9781118852538.ch8>

Geshi N, Browning J, Kusumoto S (2020) Magmatic overpressures, volatile exsolution and potential explosivity of fissure eruptions inferred via dike aspect ratios. *Sci Rep* 10:1–9. <https://doi.org/10.1038/s41598-020-66226-z>

Gibson SA, Geist DG, Day JA, Dale CW (2012) Short wavelength heterogeneity in the Galápagos plume: Evidence from compositionally diverse basalts on Isla Santiago. *Geochemistry Geophysics Geosystems* 13(9). <https://doi.org/10.1029/2012GC004244>

Goehring BM, Kurz MD, Balco G, Schaefer JM, Licciardi J, Lifton N (2010) A reevaluation of in situ cosmogenic ^3He production rates. *Quaternary Geochron* 5:410–418. <https://doi.org/10.1016/j.quageo.2010.03.001>

Grant PR, Boag PT (1980) Rainfall on the Galápagos and the demography of Darwin’s finches. *Auk* 97:227–244. <https://doi.org/10.1093/auk/97.2.227>

Grant JV, Kattenhorn SA (2004) Evolution of vertical faults at an extensional plate boundary, southwest Iceland. *J Struct Geo* 26:537–557. <https://doi.org/10.1016/j.jsg.2003.07.003>

Gregg PM, Le Mével H, Zhan Y, Dufek J, Geist D, Chadwick WW (2018) Stress triggering of the 2005 eruption of Sierra Negra Volcano, Galápagos. *Geophys Res Lett* 45:13,288–13,297. <https://doi.org/10.1029/2018GL080393>

Gudmundsson A (2012) Magma chambers: Formation, local stresses, excess pressures, and compartments. *J Volcanol Geotherm Res* 237–238:19–41. <https://doi.org/10.1016/j.jvolgeores.2012.05.015>

Harpp KS, Geist DJ (2018) The evolution of Galápagos Volcanoes: An Alternative Perspective. *Front Earth Sci* 6:1–16. <https://doi.org/10.3389/feart.2018.00050>

Harpp KS, Wanless VD, Otto RH, Hoernle K, Werner R (2005) The Cocos and Carnegie Aseismic Ridges: A Trace Element Record of

Long-Term Plume-Spreading Center Interaction. *J Petrol* 46:109–133. <https://doi.org/10.1093/petrology/egh064>

Harpp KS, Geist D, Koleszar AM, Christensen B, Lyons J, Sabga M, Rollins N (2014) The geology and geochemistry of Isla Floreana, Galápagos: A different type of late-stage ocean island volcanism. *Galápagos Nat. Lab Earth Sci in AGU Monogr* 204:71–118

Hooft EEE, Toomey DR, Solomon SC (2003) Anomalously thin transition zone beneath the Galápagos hotspot. *Earth Planet Sci Lett* 216:55–64. [https://doi.org/10.1016/S0012-821X\(03\)00517-X](https://doi.org/10.1016/S0012-821X(03)00517-X)

Huppert KL, Perron JT, Royden LH (2020) Hotspot swells and the lifespan of volcanic ocean islands. *Sci Adv* 6:eaaw6906. <https://doi.org/10.1126/sciadv.aaw6906>

Huppert HE, Woods AW (2002) The role of volatiles in magma chamber dynamics. *Nature* 420:493–495. <https://doi.org/10.1038/nature01211>

Kuiper YD (2002) The interpretation of inverse isochron diagrams in $^{40}\text{Ar}/^{39}\text{Ar}$ geochronology. *Earth Planet Sci Lett* 203:499–506. [https://doi.org/10.1016/S0012-821X\(02\)00833-6](https://doi.org/10.1016/S0012-821X(02)00833-6)

Kurz MD (1986) Cosmogenic helium in a terrestrial igneous rock. *Nature* 320:435–439. <https://doi.org/10.1038/320435a0>

Kurz MD (1986) In situ production of terrestrial cosmogenic helium and some applications to geochronology. *Geochim Cosmochim Acta* 50:2855–2862. [https://doi.org/10.1016/0016-7037\(86\)90232-2](https://doi.org/10.1016/0016-7037(86)90232-2)

Kurz MD, Geist D (1999) Dynamics of the Galapagos hotspot from helium isotope geochemistry. *Geochim Cosmochim Acta* 63:4139–4156. [https://doi.org/10.1016/S0016-7037\(99\)00314-2](https://doi.org/10.1016/S0016-7037(99)00314-2)

Kurz MD, Kenna TC, Lassiter JC, DePaolo DJ (1996) Helium isotopic evolution of Mauna Kea volcano: First results from the 1-km drill core. *J Geophys Res Solid Earth* 101:11781–11791. <https://doi.org/10.1029/95JB03345>

Kurz MD, Rowland SK, Curtice J, Saal AE, Naumann T (2014) Eruption rates for Fernandina volcano: a new chronology at the Galápagos hotspot center. In: Harpp K, Mittelstaedt E, d’Ozouville N, Graham DW (eds) *The Galápagos: A Natural Laboratory for the Earth Sciences*, Geophysical Monograph Series 204 pp 41–54. <https://doi.org/10.1002/9781118852538.ch4>

Lal D (1991) Cosmic ray labeling of erosion surfaces: in situ nuclide production rates and erosion models. *Earth Planet Sci Lett* 104:424–439. [https://doi.org/10.1016/0012-821X\(91\)90220-C](https://doi.org/10.1016/0012-821X(91)90220-C)

Le Corvec N, Walter TR (2009) Volcano spreading and fault interaction influenced by rift zone intrusions: Insights from analogue experiments analyzed with digital image correlation technique. *J Volcanol Geotherm Res* 183:170–182. <https://doi.org/10.1016/j.jvolgeores.2009.02.006>

Lietz J, Schmincke HU (1975) Miocene—pliocene sea-level changes and volcanic phases on gran Canaria (Canary islands) in the light of new K—Ar ages. *Palaeogeogr Palaeoclimatol Palaeoecol* 18(3):213–239. [https://doi.org/10.1016/0031-0182\(75\)90034-6](https://doi.org/10.1016/0031-0182(75)90034-6)

Lifton N, Sato T, Dunai TJ (2014) Scaling in situ cosmogenic nuclide production rates using analytical approximations to atmospheric cosmic-ray fluxes. *Earth Planet Sci Lett* 386:149–160. <https://doi.org/10.1016/j.epsl.2013.10.052>

Luttrell K, Sandwell D (2010) Ocean loading effects on stress at near shore plate boundary fault systems. *J Geophys Res Solid Earth* 115:1–14. <https://doi.org/10.1029/2009JB006541>

Mackey BH, Quigley MC (2014) Strong proximal earthquakes revealed by cosmogenic ^3He dating of prehistoric rockfalls, Christchurch, New Zealand. *Geology* 42:975–978. <https://doi.org/10.1130/G36149.1>

Martel SJ, Langley JS (2006) Propagation of normal faults to the surface in basalt, Koae fault system. *Hawaii J Struct Geol* 28:2123–2143. <https://doi.org/10.1016/j.jsg.2005.12.004>

Martin LC, Blard PH, Balco G, Lavé J, Delunel R, Lifton N, Laurent V (2017) The CREp program and the ICE-D production rate calibration database: A fully parameterizable and updated online tool to compute cosmic-ray exposure ages. *Quat Geochronol* 38:25–49. <https://doi.org/10.1016/j.quageo.2016.11.006>

McBirney AR, Williams H (1969) Geology and petrology of the Galápagos Islands. *GSA Memoirs* 118:1–197. <https://doi.org/10.1130/MEM118-p1>

McGuire WJ (1996) Volcano instability: a review of contemporary themes. *Geol Soc Lond Spec Publ* 110(1):1–23. <https://doi.org/10.1144/GSL.SP.1996.110.01.01>

McGuire WJ, Howarth RJ, Firth CR, Solow AR, Pullen AD, Saunders SJ, Stewart IS, Vita-Finzi C (1997) Correlation between rate of sea-level change and frequency of explosive volcanism in the Mediterranean. *Nature* 389(6650):473–476. <https://doi.org/10.1038/38998>

Medynski S, Pik R, Burnard P, Dumont S, Grandin R, Williams A, Blard PH, Schimmelpfennig I, Vye-Brown C, France L, Ayalew D (2016) Magmatic cycles pace tectonic and morphological expression of rifting (Afar depression, Ethiopia). *Earth Planet Sci Lett* 446:77–88

Mittelstaedt E, Soule S, Harpp K, Fornari D, McKee C, Tivey M, Geist D, Kurz MD, Sinton C, Mello C (2012) Multiple expressions of plume-ridge interaction in the Galápagos: Volcanic lineaments and ridge jumps. *Geochem Geophys Geosyst* 13:1–31. <https://doi.org/10.1029/2012GC004093>

Montgomery-Brown EK, Miklius A (2021) Periodic dike intrusions at Kīlauea volcano, Hawai’i. *Geology* 49:397–401. <https://doi.org/10.1130/G47970.1>

Neves MC, Bott MHP, Searle RC (2004) Patterns of stress at midocean ridges and their offsets due to seafloor subsidence. *Tectonophysics* 386:223–242. <https://doi.org/10.1016/j.tecto.2004.06.010>

Orellana-Rovirosa F, Richards M (2018) Emergence/Subsidence Histories Along the Carnegie and Cocos Ridges and Their Bearing Upon Biological Speciation in the Galápagos. *Geochem Geophys Geosyst* 19:4099–4129. <https://doi.org/10.1029/2018GC007608>

Peacock DCP, Parfitt EA (2002) Active relay ramps and normal fault propagation on Kilauea Volcano. *Hawaii J Struct Geol* 24:729–742. [https://doi.org/10.1016/S0191-8141\(01\)00109-2](https://doi.org/10.1016/S0191-8141(01)00109-2)

Pinel V, Jaupart C (2000) The effect of edifice load on magma ascent beneath a volcano. *Phil Trans R Soc A* 358:1515–1532. <https://doi.org/10.1098/rsta.2000.0601>

Pinel V, Jaupart C (2003) Magma chamber behavior beneath a volcanic edifice. *J Geophys Res Solid Earth* 108:1–17. <https://doi.org/10.1029/2002JB001751>

Porter SC (1972) Distribution, Morphology, and Size Frequency of Cinder Cones on Mauna Kea Volcano. *Hawaii GSA Bull* 83:3607–3612. [https://doi.org/10.1130/0016-7606\(1972\)83%5B3607:DMASFO%5D2.0.CO;2](https://doi.org/10.1130/0016-7606(1972)83%5B3607:DMASFO%5D2.0.CO;2)

Protin M, Blard PH, Marrocchi Y, Mathon F (2016) Irreversible adsorption of atmospheric helium on olivine: A lobster pot analogy. *Geochim Cosmochim Acta* 179:76–88. <https://doi.org/10.1016/j.gca.2016.01.032>

Ramalho RS, Quartau R, Trenhaile AS, Mitchell NC, Woodroffe CD, Ávila SP (2013) Coastal evolution on volcanic oceanic islands: A complex interplay between volcanism, erosion, sedimentation, sea-level change and biogenic production. *Earth Sci Rev* 127:140–170. <https://doi.org/10.1016/j.earscirev.2013.10.007>

Ramalho RS, Quartau R, Hóskuldsson Á, Madeira J, da Cruz JV, Rodrigues A (2020) Evidence for late Pleistocene volcanism at Santa Maria Island, Azores? *J Volcanol Geoth Res* 394:106829. <https://doi.org/10.1016/j.jvolgeores.2020.106829>

Rubin AM (1992) Dike-induced faulting and graben subsidence in volcanic rift zones. *J Geophys Res Solid Earth* 97:1839–1858. <https://doi.org/10.1029/91JB02170>

Ruch J, Wang T, Xu W, Hensch M, Jónsson S (2016) Oblique rift opening revealed by reoccurring magma injection in central Iceland. *Nature Comm* 7:1–7. <https://doi.org/10.1038/ncomms12352>

Ryan WB, Carbotte SM, Coplan JO, O’Hara S, Melkonian A, Arko R, Weissel RA, Ferrini V, Goodwillie A, Nitsche F, Bonczkowski J (2009) Global multi-resolution topography synthesis. *Geochem Geophys Geosyst* 10(3). <https://doi.org/10.1029/2008GC002332>

Samrock LK, Wartho JA, Hansteen TH (2019) 40Ar-39Ar geochronology of the active phonolitic Cadamosto Seamount, Cape Verde. *Lithos* 344:464–481. <https://doi.org/10.1016/j.lithos.2019.07.003>

Schwartz DM, Soule SA, Wanless VD, Jones MR (2018) Identification of Erosional Terraces on Seamounts: Implications for Interisland Connectivity and Subsidence in the Galápagos Archipelago. *Front Earth Sci* 6:1–17. <https://doi.org/10.3389/feart.2018.00088>

Stone JO (2000) Air pressure and cosmogenic isotope production. *J Geophys Res Solid Earth* 105:23753–23759. <https://doi.org/10.1029/2000JB900181>

Swanson FJ, Batis HW, Lexa J, Dymond J (1974) Geology of Santiago, Rábida, and Pinzón Islands, Galápagos. *GSA Bull* 85:1803–1810. [https://doi.org/10.1130/0016-7606\(1974\)85%3c1803:GOSRAP%3e2.0.CO;2](https://doi.org/10.1130/0016-7606(1974)85%3c1803:GOSRAP%3e2.0.CO;2)

Takada A (1994) The influence of regional stress and magmatic input on styles of monogenetic and polygenetic volcanism. *J Geophys Res Solid Earth* 99:13563–13573. <https://doi.org/10.1029/94JB00494>

Trippanera D, Acocella V, Ruch J, Abebe B (2015) Fault and graben growth along active magmatic divergent plate boundaries in Iceland and Ethiopia. *Tectonics* 34:2318–2348. <https://doi.org/10.1002/2015TC003991>

Uppala SM, Kållberg PW, Simmons AJ, Andrae U, Bechtold VD, Fiorino M, Gibson JK, Hinesley J, Hernandez A, Kelly GA, Li X (2005) The ERA-40 re-analysis. *Q J R Meteorol Soc A J Atmos Sci Appl Meteorol Phys Oceanogr* 131(612):2961–3012. <https://doi.org/10.1256/qj.04.176>

Vigouroux N, Williams-Jones G, Chadwick W, Geist D, Ruiz A, Johnson D (2008) 4D gravity changes associated with the 2005 eruption of Sierra Negra volcano, Galápagos. *Geophysics* 73:WA29–WA35. <https://doi.org/10.1190/1.2987399>

Villagómez DR, Toomey DR, Hoot EEE, Solomon SC (2007) Upper mantle structure beneath the Galápagos Archipelago from surface wave tomography. *J Geophys Res Solid Earth* 112:1–25. <https://doi.org/10.1029/2006JB004672>

Villagómez DR, Toomey DR, Geist DJ, Hoot EEE, Solomon SC (2014) Mantle flow and multistage melting beneath the Galápagos hotspot revealed by seismic imaging. *Nature Geosci* 7:151–156. <https://doi.org/10.1038/ngeo2062>

Walter TR, Troll VR, Cailleau B, Belousov A, Schmincke H-U, Amelung F, Bogaard P (2005) Rift zone reorganization through flank instability in ocean island volcanoes: an example from Tenerife, Canary Islands. *Bull Volcanol* 67:281–291. <https://doi.org/10.1007/s00445-004-0352-z>

Watterson J (1986) Fault dimensions, displacements and growth. *Pure Applied Geophys* 124:365–373. <https://doi.org/10.1007/BF00875732>

Weissel JK, Karner GD (1989) Flexural uplift of rift flanks due to mechanical unloading of the lithosphere during extension. *J Geophys Res Solid Earth* 94:13919–13950. <https://doi.org/10.1029/JB094iB10p13919>

Werner R, Hoernle K, Barckhausen U, Hauff F (2003) Geodynamic evolution of the Galápagos hot spot system (Central East Pacific) over the past 20 m.y.: Constraints from morphology, geochemistry, and magnetic anomalies. *Geochem Geophys Geosyst* 4:1–28. <https://doi.org/10.1029/2003GC000576>

White WM, McBirney AR, Duncan RA (1993) Petrology and geochemistry of the Galápagos Islands: Portrait of a pathological mantle plume. *J Geophys Res Solid Earth* 98:19533–19563. <https://doi.org/10.1029/93JB02018>

Wilson EL, Harpp KS, Schwartz DM, Van Kirk R (2022) The Geochemical Evolution of Santa Cruz Island, Galápagos Archipelago. *Front Earth Sci* <https://doi.org/10.3389/feart.2022.845544>

Wilson DS, Hey RN (1995) History of rift propagation and magnetization intensity for the Cocos-Nazca spreading Center. *J Geophys Res Solid Earth* 100:10041–10056. <https://doi.org/10.1029/95JB00762>

Wyrick D, Ferrill DA, Morris AP, Colton SL, Sims DW (2004) Distribution, morphology, and origins of Martian pit crater chains. *J Geophys Res Planets* 109:1–20. <https://doi.org/10.1029/2004JE002240>